Isothermal-expansion melting of two-dimensional colloidal monolayers on the surface of water

1989 J. Phys.: Condens. Matter 1 1707

(http://iopscience.iop.org/0953-8984/1/9/015)

J. Phys.: Condens. Matter 1 (1989) 1707–1730. Printed in the UK

Isothermal-expansion melting of two-dimensional colloidal monolayers on the surface of water

A J Armstrong, R C Mockler and W J O'Sullivan
Condensed Matter Laboratory, Department of Physics, University of Colorado, Boulder, CO 80309, USA

Received 22 December 1987, in final form 5 October 1988

Abstract. Monodisperse distributions of 1.01 μm and 2.88 μm polystyrene microspheres in monolayers on the surface of water were used in a study of isothermal-expansion melting in two dimensions. The equation of state, defect structures, and the translational and orientational correlation functions were obtained from digitised particle positions as the particle-number density ranged from the ordered solid to the liquid phase. The 2.88 μm system showed evidence of defect mediated melting and of an intermediate hexatic phase, in partial accord with the theoretical results of Kosterlitz, Thouless, Halperin, Nelson and Young. Melting in the 1.01 μm system appeared to proceed by a weak first-order transition. If so, the difference in melting behaviour of the two samples may reflect differences in defect core creation energies which can be traced to sphere size.

1. Introduction

Monolayers of charged colloidal particles trapped in suspensions or constrained to a free water surface have been proposed as analogues of two dimensional (2D) condensed-phase atomic systems. The special interest in colloidal monolayers derives from their ability to replicate melting and crystallisation phenomena in 2D, while having the useful feature that positions and trajectories of individual particles can be monitored using microscopy in combination with digital image processing (see figure 1).

Interest in 2D melting has centred around the theory of defect-mediated melting first described by Kosterlitz and Thouless [1, 2] and later expanded upon by Halperin and Nelson [3, 4] and Young [5]. Kosterlitz and Thouless suggested that a 2D solid would exhibit quasi-long range (QLR) order characterised by power-law decay of the translational correlation function, which would switch over to exponential decay in the liquid phase. Noting that a small number of paired dislocations exist in a 2D solid well below the melting transition, they proposed that the solid might melt as a result of the thermal unbinding of these bound dislocations. The transition would be continuous (second order) and would occur at a temperature T_m at which bound dislocation pairs move apart sufficiently to screen similar pairs, allowing these to unbind. Halperin and Nelson noted, in agreement with Mermin's [6] earlier observation, that long-range bond-angle order could exist in 2D, and if the Kosterlitz–Thouless mechanism were correct, then melting should occur in two stages. Rather than becoming a liquid immediately above T_m the system should first enter a hexatic phase having short-range translational order and QLR

0953-8984/89/091707 + 24 $02.50

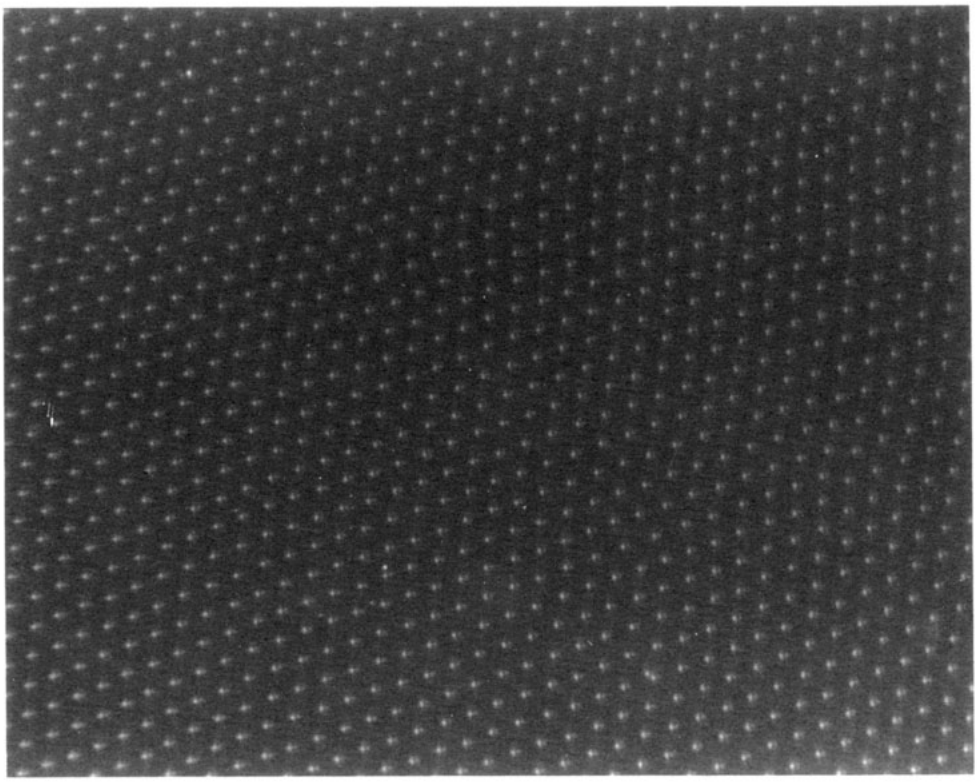

Figure 1. A photomicrograph of a colloidal monolayer of 2.88 μm microspheres on the surface of water. The interparticle spacing is 5.6 μm ($N \simeq 500$, with reference to figure 4).

orientational order, eventually converting to a liquid phase at some higher temperature when disclination pairs unbind. While other theories have been suggested [7, 8], it is the Kosterlitz–Thouless–Halperin–Nelson–Young (KTHNY) model with its novel prediction of an intermediate hexatic phase that has received the most attention.

Although no consensus has emerged, the results from many computer simulations find that 2D melting occurs via a first-order transition. This is supported by the appearance of hysteresis and discontinuities in the internal energy, and by the observation of van der Waals loops in plots of pressure against density. (For a current review of computer simulations and experiments in 2D melting see [9].) Also, particle-trajectory plots show areas of local disorder enclosed within ordered regions, suggestive of a two-phase coexistence regime near the transition temperature. The observed discontinuities or loops are small, indicating that the transition is only weakly first order [10]. Since the KTHNY mechanism is a long-wavelength theory, the finite size and imposed periodicity of the computer simulations may obscure the true nature of the transition, although simulations on relatively large particle systems [11, 12] suggest that this is not the case.

The results of experiments on 2D systems are ambiguous as to the order of the phase transition. Experiments on 2D systems of electrons on the surface of liquid helium [13] have found that the elastic response of the system goes to zero at the predicted dislocation-pair-unbinding temperature T_m, in good agreement with the KTHNY theory. Experiments on rare-gas films on the surface of graphite [14–16] and on monolayers of organic molecules on the surface of water [17, 18] have had mixed results. For xenon on

the surface of graphite Rosenbaum and co-workers [14] and Heiney and co-workers [15] found results consistent with the KTHNY theory, although the latter were unable to rule out the possibility of two-phase coexistence. More recently Nagler and co-workers [16] have examined the same system. While their results were consistent with the existence of an hexatic phase, they suggest that until the effects of the substrate orienting field are better understood experiments of this type cannot be conclusive. Results of experiments on freely suspended liquid crystals [19, 20] indicate a first order transition. Recent work by Murray and Van Winkle [21] and Tang and co-workers [22] on systems of polystyrene colloidal particles trapped between two glass plates found the behaviour of the translational and orientational correlation functions to be consistent with a two-stage process, although Tang was unable to rule out the possibility of two-phase coexistence.

In view of these differences, several authors have re-examined the KTHNY mechanism, paying particular attention to the role of the core energy required to create a tightly bound pair of dislocations. Saito [23] has conducted a Monte Carlo simulation which considers only the dislocation creation, annihilation and diffusion probabilities for varying values of the core creation energy. He finds that for large values of the core energy the system follows the KTHNY theory, while for small values of the core energy the transition becomes first order. Kleinert [24, 25] has examined the problem using a gauge-field theory approach and finds that variations in core energy will cause the transition to switch from first to second order in a manner consistent with the simulation of Saito [23].

In this paper we present the results of a study of isothermal-expansion melting in colloidal microsphere monolayers on the surface of water. In § 2 we describe the experimental system, the data analysis and the chosen model for the pair interaction. From the particle positions and the model-pair interaction, the equation of state, the defect structure and the correlation functions are determined. The experimental results for two different sphere diameters, 1.01 μm and 2.88 μm, are presented in § 3. For each size the calculated equation of state is fitted in the low-density region with a power series in particle number. The 2.88 μm system shows an intermediate orientationally ordered (hexatic) phase, while the nature of the transition for the 1.01 μm system is uncertain. In § 4 we discuss the phase transitions for the two different systems. We suggest that the 1.01 μm system may melt via a first-order transition and the contrast between the two systems may be ascribed to differences in their respective values of the core creation energy as suggested by Saito [23].

2. Experimental system

2.1. Apparatus and procedure

Samples are formed on an ultra-clean water surface in a $19 \times 3.8 \times 1$ cm^3 anodised-aluminum Langmuir trough dyed black and coated with a thin film of Teflon. The trough is mounted in an isolation box containing supports for two Teflon barriers used to sweep the surface clean and to compress the sample. The barriers are driven by lead screws attached to a 5000 : 1 reduction DC motor. The entire apparatus is mounted on a microscope equipped with a motor-driven translation stage and a video camera connected to a video-cassette recorder.

Highly-uniform monodisperse polystyrene microspheres, 0.1–5.0 μm in diameter, are commercially available and have long been used to produce classical analogues of

three-dimensional crystals [26]. Attached to and uniformly distributed over the surface of the spheres are sulphate polar head groups. When immersed in water the sulphate groups dissociate leaving a net negative charge on the sphere and a hydrogen-ion cloud surrounding it. The spheres are carefully cleaned to remove any residual surfactants and ions by repeated centrifuging with methanol. Cleaning is critical, since the presence of any surfactant, either in the sphere–methanol suspension or on the free-water surface, will inhibit the formation of crystals.

Samples are prepared by overfilling the trough so that a large meniscus is present to enable formation of a good seal between the trough and the barriers. The surface is swept with the barriers to remove any residual surface contaminants. The entire apparatus is allowed to equilibrate to room temperature, which is maintained to ± 1 °C during the experiment. The spheres are deposited by allowing several drops of the sphere–methanol suspension to flow down a clean glass rod penetrating the water surface. The suspension spreads over the surface and very little material is transferred to the bulk. The methanol either evaporates or is absorbed into the water, leaving the spheres trapped on the surface by electrostatic and surface-tension forces [27, 28].

A successful transfer of the microspheres to the water surface will yield a monolayer consisting primarily of monodisperse particles with a fraction of a percent of multiparticle clusters (two or three spheres sticking together). If improperly prepared, the percentage of multiparticle clusters will be high, and the formation of crystals will be inhibited. Severe contamination will yield a 2D glass or, in some cases, circular islands of crystal surrounded by the contaminant. The concentration of multiparticle defects appears to be independent of the initial density deposited on the surface and seems to depend only on the cleanliness of the system. At present we lack sufficient data to give a clear picture of the effect of these multiparticle contaminants. Qualitatively it appears that they pin grain boundaries and thus limit the grain size in the solid state; the larger the percentage of multiparticle defects, the smaller the resulting grains in the solid.

A video tape is made of the entire compression–expansion history of the system. Selected images from the video tape are digitised with a 512×480 pixel digitiser and stored on disc for later processing. Images are processed with a series of image-enhancing filters to correct for noise and non-uniform illumination [29]. The total 2D area sampled after the images are processed is 6.73×10^{-4} cm^2. The particle number observed in this area ranges from 600 (8.9×10^5 particles cm^{-2}) in the low-density gaseous regime to approximately 6000 (8.9×10^6 particles cm^{-2}) in the high-density crystalline regime. This gives a variation in interparticle separation ranging from approximately 4 to 12 μm. From the processed images the position of the centre of mass of the individual spheres is located and stored. The configurational thermodynamics, defect structures and correlation functions are determined from the centre-of-mass data.

2.2. The systems examined

The 2.88 μm monolayer was deposited on the surface at a relatively high density, with the barriers confining the spheres within half of the total area of the trough. The total number of particles on the surface was estimated to be $\simeq 3 \times 10^7$ and the multiparticle cluster count was approximately three per thousand particles. The sample showed initial density variations across the surface and was allowed to equilibrate for one day. Then it was examined and found to be homogeneous across the surface, except near the edges of the trough, where the curvature of the meniscus causes a substantial density gradient due to compression by the gravitational field. Two compression–expansion cycles for

this system are analysed here. The sample was compressed–expanded at approximately 80–100 μm per minute for ten-minute periods or until each barrier had advanced 1 mm (800–1000 μm). Between these periods the system was allowed to relax for 45 to 60 minutes before the compression–expansion was continued. In some cases it was allowed to rest longer, several hours or overnight, with no observable differences from the 60 min relaxation periods.

After several days the sample started to accumulate additional large clustered defects and vacant regions, indicating the presence of surface contaminates attributable to possible leaching from the trough or from airborne particulates. This limits the useful sample life to about one week.

Two 1.01 μm samples, designated 101A and 101B, were analysed under compression only. Sample 101A was deposited at low density with both barriers completely retracted so that the monolayer covered the entire trough. The estimated number of particles on the surface was $\simeq 3 \times 10^7$ and the multiparticle cluster count was approximately 12 per thousand particles. The sample was allowed to equilibrate for one day, after which an examination of the surface showed a uniform distribution of particles. This monolayer was compressed at a rate of 80 to 100 μm min^{-1} for three successive three-hour periods, with intervals of five and thirteen hours between compressions. During this time no detectable density gradients were observed over the surface except for the normal density gradients at the edges where the meniscus curves sharply. Also, near the barriers in the direction of their advance, a density gradient was observed that extended beyond that normally caused by the meniscus. The compression was continued until many large-aggregate close-packed rafts of particles (50–100 in number) formed. At this point the monolayer was no longer useful and was discarded.

The second sample, 101B, was made under similar circumstances. The total number of particles in the monolayer was estimated to be $\simeq 4 \times 10^7$, with a cluster defect count of nine per thousand particles. After equilibrating for one day the sample was uniform over the surface. The system was compressed at 20 μm min^{-1} continuously for two intervals of two and three hours respectively, with a twelve-hour relaxation period between them. It was then completely expanded and allowed to equilibrate for one day, after which the surface was re-examined. Over its flat portions the monolayer was gas-like, while at the edges, within the curvature of the meniscus, the system varied from a gas to a highly ordered crystalline solid phase adjoining the trough edge. Data were taken from a scan of this gradient region. The profile of the surface was found by moving the stage a known amount and measuring the vertical distance needed to bring the surface back into focus.

2.3. *The pair interaction and equation of state*

The 2D pair interaction energy for microspheres in the plane of the air–water interface can be separated into two parts

$$\varphi_t(r) = \varphi_e(r) + \varphi_c(r) \tag{1}$$

where $\varphi_e(r)$ is the electrostatic potential energy due to the dissociation of charged head groups and $\varphi_c(r)$ is a capillary interaction resulting from the distortion of the free surface by the trapped spheres. Pieranski [30] proposed that the long-range electrostatic interaction between microspheres at an air–water surface was dipolar, resulting from the asymmetric charge distribution imposed by the presence of the surface. Hurd [31],

expanding on the work of Stillinger [32], has derived the form of the dipole-pair interaction energy for two spheres on the surface of water. He finds

$$\varphi_e(r) = 2\left(\frac{Ze}{\varepsilon\kappa}\right)^2 \frac{1}{r^3} + \frac{2Z^2e^2}{\varepsilon}\frac{\varepsilon^2}{(\varepsilon^2-1)}\frac{e^{-\kappa r}}{r} \tag{2}$$

where κ is the Debye screening length for pure water, ε is the dielectric constant of water, e is the electronic charge, and Z is the number of dissociated head groups per sphere. The first term in equation (2) is the long-range dipole contribution with moment

$$p = Ze/\sqrt{\varepsilon}\kappa$$

that results from the distortion of the counterion cloud by the surface; the second term is the screened Coulomb interaction for charged particles in a bulk electrolyte corrected for the presence of the dielectric interface.

Since the capillary interaction $\varphi_c(r)$ is long range and can be either attractive or repulsive [27], it can be significant in systems of this type. However, it is found to be negligible for the sphere sizes used in this work when compared to the electrostatic terms, and we ignore it in all calculations.

Using the model interaction of equation (2) and taking the particle positions from the processed images, the equation of state can be found by direct application of the virial theorem

$$\frac{PA}{Nk_BT} = 1 - \tfrac{1}{2}\left(\left\langle \sum_{i<j}^{N} \boldsymbol{r}_{ij} \cdot \nabla\varphi(|\boldsymbol{r}_{ij}|)\right\rangle \Big/ Nk_BT\right) \tag{3}$$

where $\nabla\varphi(|\boldsymbol{r}_{ij}|)$ is the gradient of the pair interaction in equation (2) and $\boldsymbol{r}_{ij}$ is the vector joining the ith and jth particles. The 2D area A used in the calculation of the equation of state is chosen near the centre of each processed image and is equal to 1.59×10^{-4} cm^2; N is the observed particle number within A. All parameters are known in equation (2) except Z, which depends on the spheres' wetted surface area and on the fraction of dissociated head groups, so it is convenient to calculate the configurational part of the equation of state divided by Z^2, giving

$$(PA - Nk_BT)/Z^2 = -\tfrac{1}{2}\left\langle \sum_{i>j}^{N} \boldsymbol{r}_{ij} \cdot \nabla\varphi'(|\boldsymbol{r}_{ij}|)\right\rangle \tag{4}$$

where

$$\varphi'(r) = \varphi(r)/Z^2.$$

3. Results

3.1. Equation of state

The configurational component of the equation of state for sample 101A and a log–log version of the same are shown in figures 2 and 3, respectively. The densities covered range from a gas to a highly ordered polycrystalline solid phase. Each point represents a single frame from the video tape of a gaseous-to-solid compression. The inherent error introduced by the uncertainty in particle separations, ± 1 pixel or $\simeq \pm 0.5$ μm, is obscured by the size of the data points and is much smaller than the statistical scatter of the

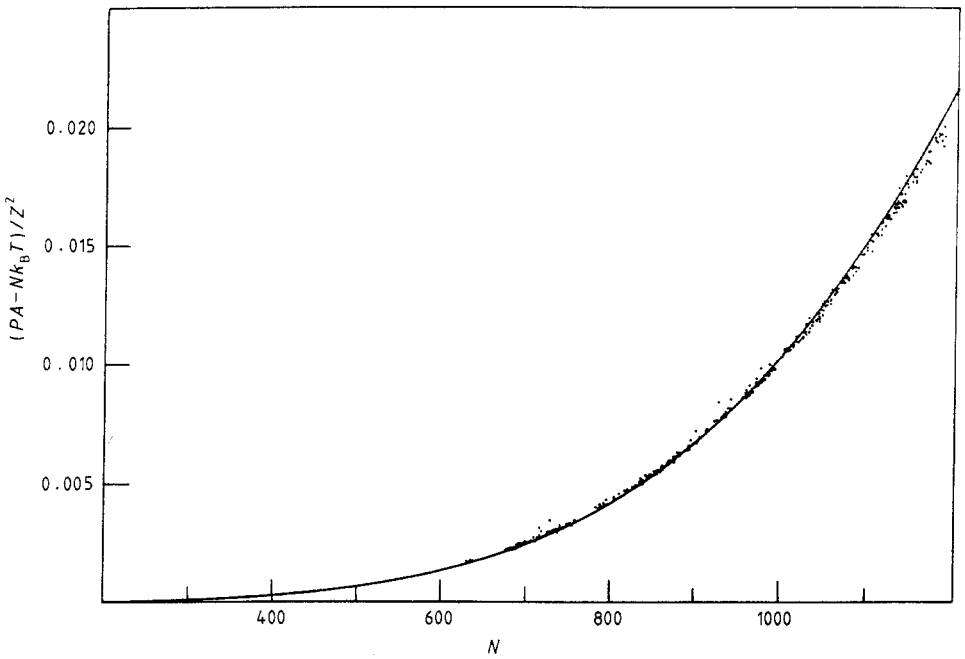

Figure 2. The configurational component of the equation of state divided by Z^2 for sample 101A (1.01 μm particles). The number of particles in an area of 1.59×10^{-4} cm^2 near the centre of the video image determines the particle number (N) of the x axis. The solid line is the fit calculated from the low-density virial expansion: points in the very low density regime are obscured by the fit. In this figure and in figures 3 and 4 each point is from a single video frame. The error introduced from the uncertainty in particle positions is smaller than the point size.

individual frame values. Since each point represents only one configuration, the results presented here do not comprise an actual equation of state. Strictly speaking, each piece of data should be an average over many uncorrelated frames: however, this is computationally impractical with our computer capability. The narrowness of the scatter in figures 2 and 3 suggests that the single-frame data provide a useful approximation to the actual equation of state within the experimental resolution.

The equation of state can be written as a power series in particle number given by

$$\frac{(PA - Nk_BT)}{Z^2} = k_BT\sum_{i=2}^{\infty} B_iN^i. \tag{5}$$

For a dilute gas only the first few terms will contribute significantly to the sum. Fitting the low density region of figure 2 with a fourth order polynomial in N gives the approximate equation of state,

$$(PA - Nk_BT)/Z^2 = 0.432 \times 10^{-9}k_BTN^2 - 0.147 \times 10^{-11}k_BTN^3 + 0.114 \times 10^{-13}k_BTN^4 \ldots. \tag{6}$$

The experimental equation of state is seen to compare well with the low density virial expansion given by equation (6) up to $N \simeq 1000$. The solid line in figure 2 is the low-density fit of the equation of state. At higher densities the data deviate systematically

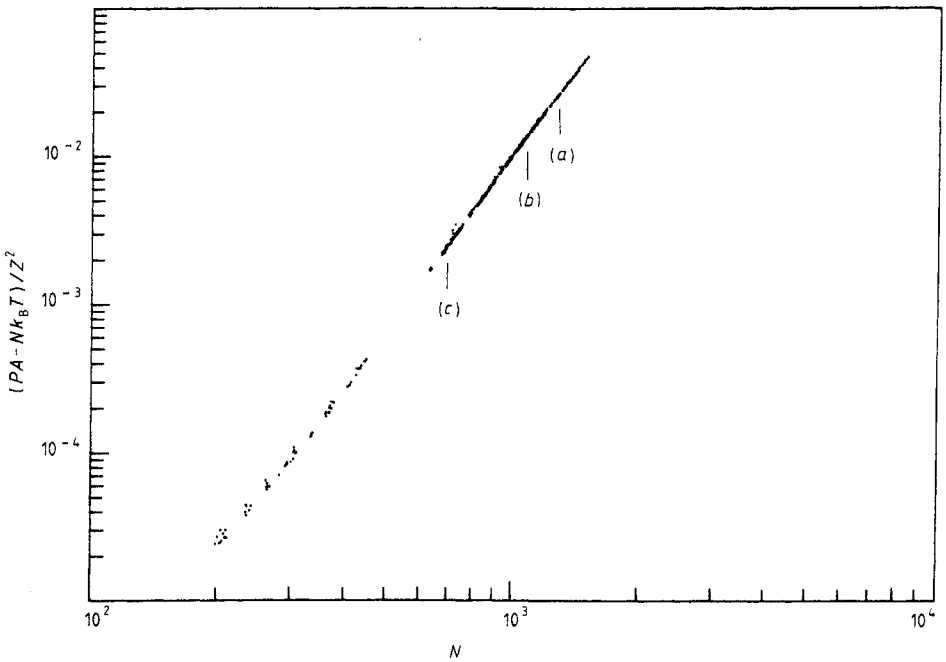

Figure 3. Log–log plot of the configurational component of the equation of state divided by Z^2 for sample 101A (1.01 μm spheres). (Positions marked (*a*), (*b*) and (*c*) relate to figure 5.)

from the low-density approximation. For low N-values the log–log plot of the same data (figure 3) shows a slight upward curvature, to a linear regime for $400 \leqslant N \leqslant 1000$, and then displays a systematic departure from linearity for $N > 1000$. This change near 1000 particles shows itself in figure 3 as a very slight alteration in slope.

The log–log plot of the equation of state for the 2.88 μm system is shown in figure 4. The densities cover the range from a disordered gaseous phase to a nearly defect-free solid. The overall shape of the curve is similar to that of sample 101A, but shows some distinct differences. In the low-density region the curve is nearly linear and is fitted well by a low-density virial expansion. The equation of state in this region is given by

$$(PA - Nk_BT)/Z^2 = 0.314 \times 10^{-9} k_B TN^2 - 0.159 \times 10^{-11} k_B TN^3 + 0.101 \times 10^{-14} k_B TN^4 \ldots . \quad (7)$$

The fit is poor at the higher densities, as was observed with sample 101A, and shows a significant systematic departure from the data for $N \geqslant 600$. For $600 \leqslant N \leqslant 1600$ the curve looks very similar to that of the 1.01 μm sample, and again, near $N \simeq 1000$ the curve makes a slight change in slope. However, the correlation functions and defect structures differ dramatically from their counterparts in the 1.01 μm systems. (See §§ 3.2 and 3.3 below.)

Broughton *et al* [10], van Swol and Woodcock [33], and Kalia and Vashishta [34] have performed molecular-dynamics simulations on systems interacting under various inverse-power potentials. They inferred the existence of a weak first-order transition from the observation of small discontinuities in the equation of state and in the internal energy, with accompanying hysteresis. We see no sign of a distinct discontinuity or van

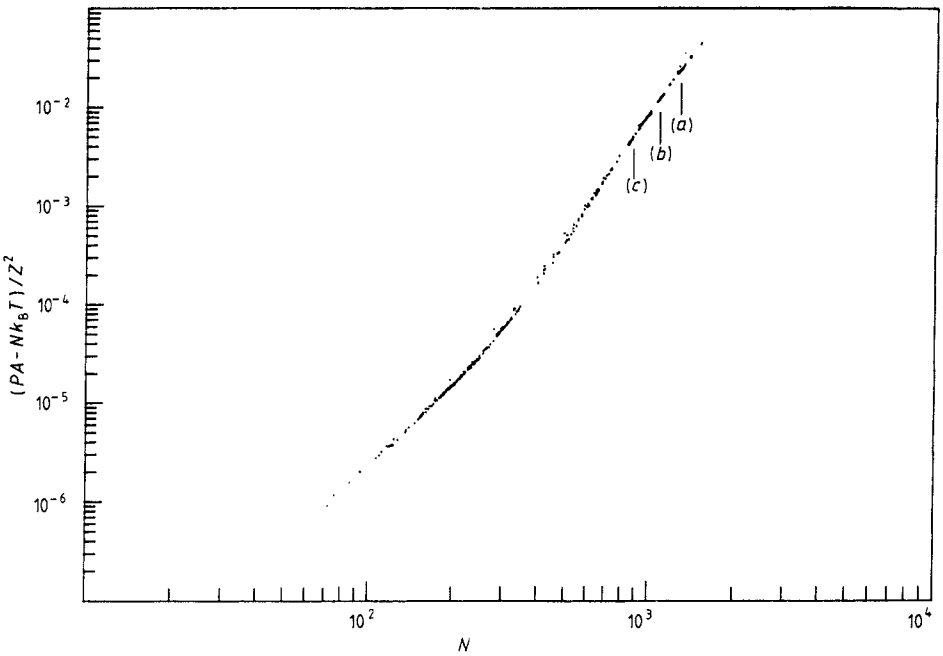

Figure 4. Log–lot plot of the configurational component of the equation of state divided by Z^2 for the 2.88 μm sample. (Positions marked (*a*), (*b*) and (*c*) relate to figure 6.)

der Waals loop in either the 1.01 μm or the 2.88 μm samples, and for the 2.88 μm sample there is no sign of hysteresis. At our magnification and for the relatively small number of particles used in these experiments the presence of any discontinuity or loop could be hidden within the resolution of the experiment.

3.2. Defect structure

Samples of the defect structure for sample 101A and the 2.88 μm system are shown in figures 5 and 6, respectively. The defect maps are constructed by finding the minimum area polygon (Wigner–Seitz cell) made by the intersection of the perpendicular bisectors of the bonds joining a particle to a set of its nearest neighbours [35]. If the number of sides of the resulting polygon is not six it is given a symbol marking its centre of mass and drawn. Five-sided polygons are shaded and the centres of seven-sided polygons are marked with a + sign; particles having six nearest neighbours have a point marking their centre of mass. Dislocations appear as contiguous five- and seven-sided polygons with the resulting Burger's vector oriented roughly normal to the line joining the polygon centres.

In figure 5 representative frames from three different density regions of sample 101A are shown. Their corresponding positions in the equation of state plot (figure 3) are marked (*a*), (*b*), and (*c*), accordingly: (*a*) is a representative frame from the polycrystalline solid; (*b*) is a frame taken near the region where the low density virial expansion no longer fits the data ($N \geqslant 1000$); and (*c*) is a frame chosen from well into the gaseous regime.

In the low-density gas phase (figure 5(*c*)) the maps show surprisingly large regions

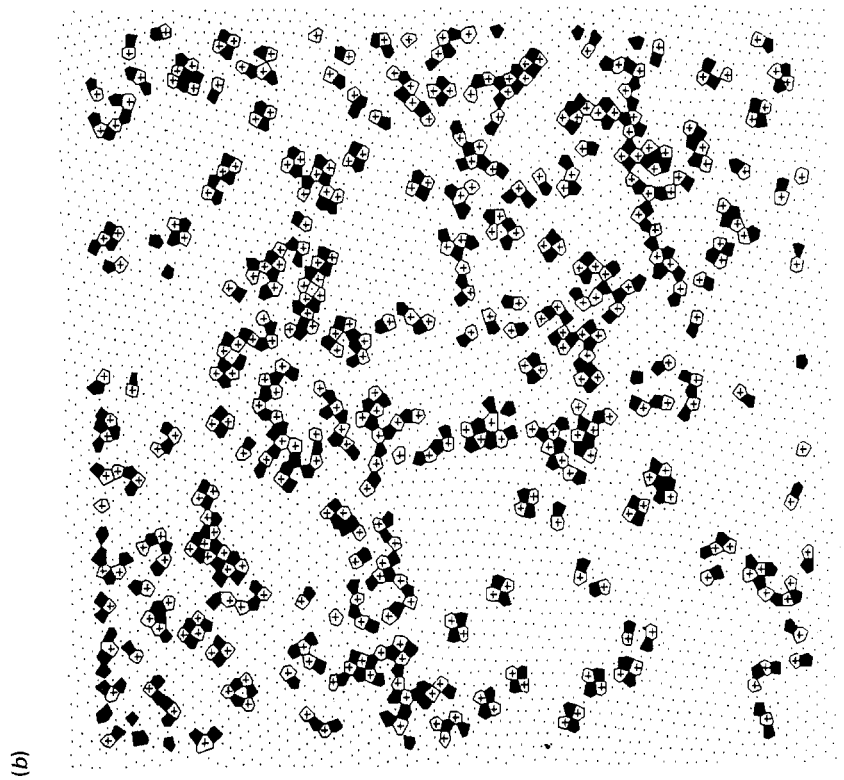

(b)

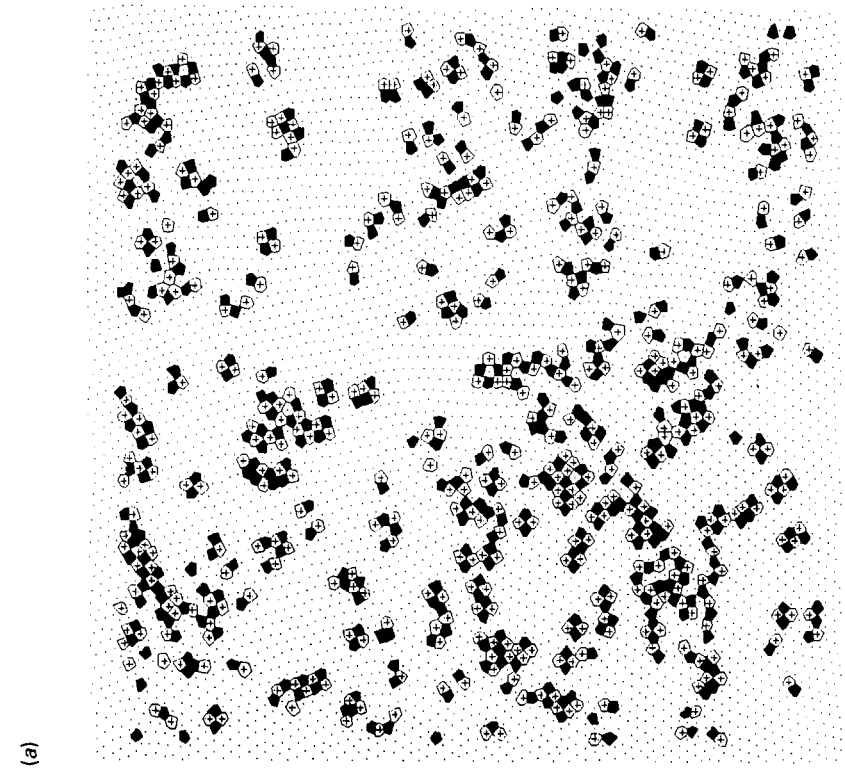

(a)

Figure 5. The defect structure from three different densities of sample 101A. Seven-sided polygons are denoted with a + and five-sided polygons are shaded. The three maps, 5(*a*), 5(*b*) and 5(*c*), are from frames near the positions marked (*a*), (*b*) and (*c*), respectively, in figure 3.

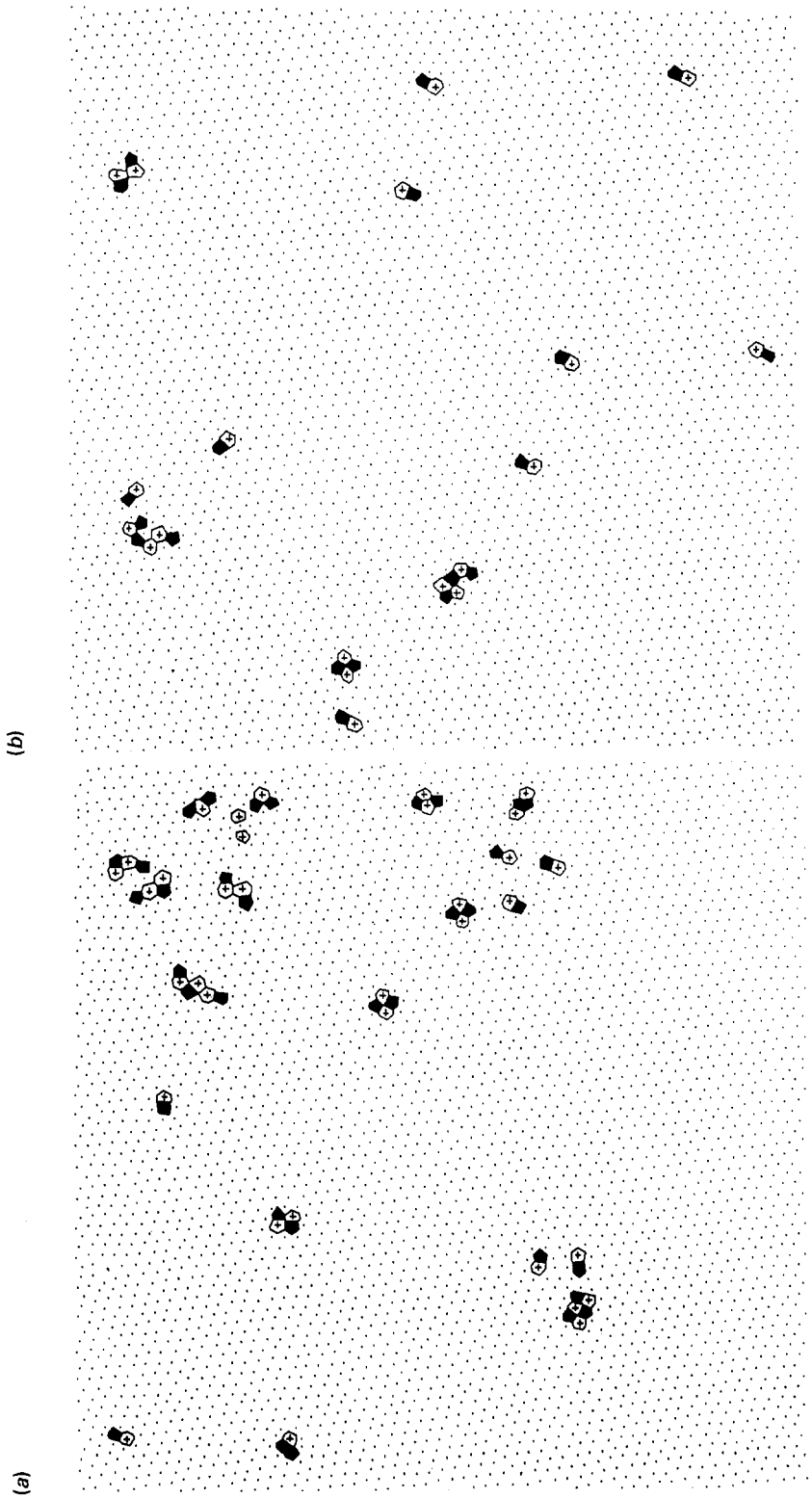
(b)
(a)

Figure 6. Samples of the defect structure of the 2.88 μm sample. The three maps, 6(*a*), 6(*b*) and 6(*c*), are from frames near the positions marked (*a*), (*b*), and (*c*), respectively, in figure 4.

with no defects; this is an often noted feature in 2D systems [10, 35]. The defects form large connected clusters that nearly span the system and sometimes completely isolate the defect-free areas from each other. Close examination of the defect-free areas show that the axes defining local regions display considerable wander and bend. The scatter in their orientation is significant enough to suggest that these regions may well be transitory. (The defect maps are representations of essentially instantaneous particle configurations.)

The defect structure near the change in slope in figure 3 (position (*b*) in figure 3) is depicted in figure 5(*b*) and differs markedly from the gas–liquid structure (figure 5(*c*)). The defect clusters have now thinned and no longer appear close to spanning the system. The defect-free areas are larger and the local axes in these regions are well defined and even appear to correlate with those in other ordered regions. At this density, tightly bound dislocation pairs are now easily seen in the ordered pools and are also seen in association with defect clusters. Since a dislocation can be thought of as two adjacent disclinations (connected five- and seven-sided polygons), the tightly bound dislocation pairs appear as quadrupoles of disclinations. (We will refer to these tightly bound pairs of dislocations as quadrupoles.) The quadrupoles have a net Burger's vector of zero and form the lowest energy configuration for two oppositely oriented dislocations. The quadrupoles in general are observed to be short lived, with their number and positions fluctuating rapidly. The proliferation of quadrupoles has been reported in many simulations [10, 23, 35].

The map of the solid phase well above the slight change in slope in the equation of state is shown in figure 5(*a*). Aside from the difference in density, figures 5(*a*) and 5(*b*) appear similar. The defect structure is almost entirely confined to small clusters or well defined strings of dislocations which mark the grain boundaries between differently oriented crystallites. The number of isolated dislocations in the interior of the crystallites is small while the number of observed quadrupoles appears large. We believe that the small grain size in the solid state of the 1.01 μm samples is the result of a large multiparticle defect count. It appears that these multiparticle defects trap dislocations between them and create the grain boundaries. Rubinstein and Nelson [36] have examined computer-generated random packing arrays of hard discs with mixed disc diameters and find similar results. They find that a single large impurity disc placed at the centre of the system traps dislocations and can, for large enough off-size diameter, give rise to arrays of stacking faults and grain boundaries.

The defect structure of the 2.88 μm system is much different (see figure 6). At low densities (not shown) it is similar to the 1.01 μm systems, except the average cluster size is smaller and defect clusters do not span the system. The fraction of six-coordinated particles F_6, defined as the number of six-sided cells divided by the total number of cells, is larger for the 2.88 μm system at all densities; in the low-density region (200 to 400 particles) F_6 is 71% for the 2.88 μm system as against 61% for 1.01 μm system. The distinctive difference in defect structure between the two systems appears in the intermediate-density region below the apparent slope change in figure 4 ($600 \leqslant N \leqslant 1000$). Figure 6(*c*) shows the defect structure of the 2.88 μm system slightly below this point (position (*c*) in figure 4). This is noticeably different from that of figure 5(*c*) for the 1.01 μm system. At these densities the system displays QLR orientational order and short-range translational order (§ 3.3). The crystal axes are well defined, implying orientational correlation among the particles over the entire frame. The dislocations are well separated with the exception of the small strings and clusters in the mid-right-hand side. The lowest defect pair in the far lower left-hand

corner of figure 6(*c*) is a vacancy. Vacancies and interstitials are often marked by a pair of closely bound dislocations offset by one lattice spacing. Vacancies have the dislocations offset such that the two seven-sided polygons are stacked on top of each other, while interstitials appear with stacked five-sided polygons. (These are not the only defect configurations that identify vacancies and interstitials.) A frame from the region marked (*b*) in figure 4 is shown in figure 6(*b*). Here the density of dislocations is reduced and it is possible to clearly distinguish some dislocation pairs. In figure 6(*a*) a frame well above the change in slope in figure 4 is shown (position (*a*) in figure 4). Here the number of defects is small (as in figure 6(*b*)) and the separation distance for coupled pairs is likewise small.

3.3. Correlation functions

The translational correlation functions,

$$g(r) = \langle \rho(r)\rho(0) \rangle$$

for selected densities of the 2.88 μm sample are shown in figure 7 and the corresponding orientational correlation functions in figure 8. Each curve is an average of correlation functions from 5 to 20 frames. The translational correlation functions have been offset for clarity; all the functions decay to unity. The orientational correlation function is given by [35]

$$g_6(r) = \langle \Psi_6(r)\Psi_6^*(0) \rangle / g(r) \tag{8}$$

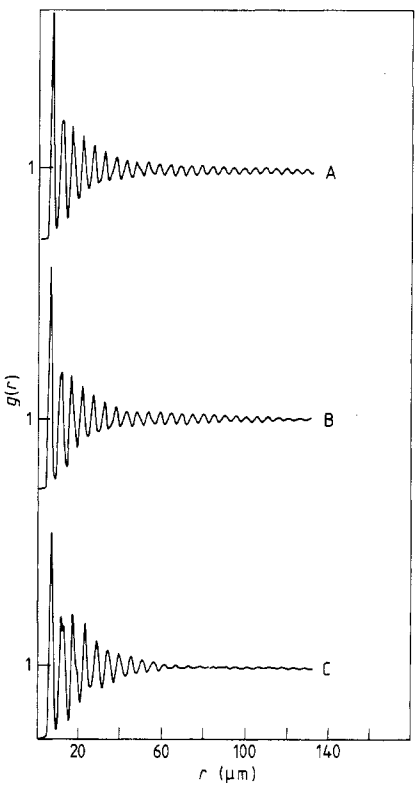

Figure 7. Samples of the average translational correlation functions $g(r)$ from the 2.88 μm sample. Each curve is the average of 5 to 20 correlation functions from individual frames. The particle numbers are: A, $N = 867$; B, $N = 829$; and C, $N = 726$.

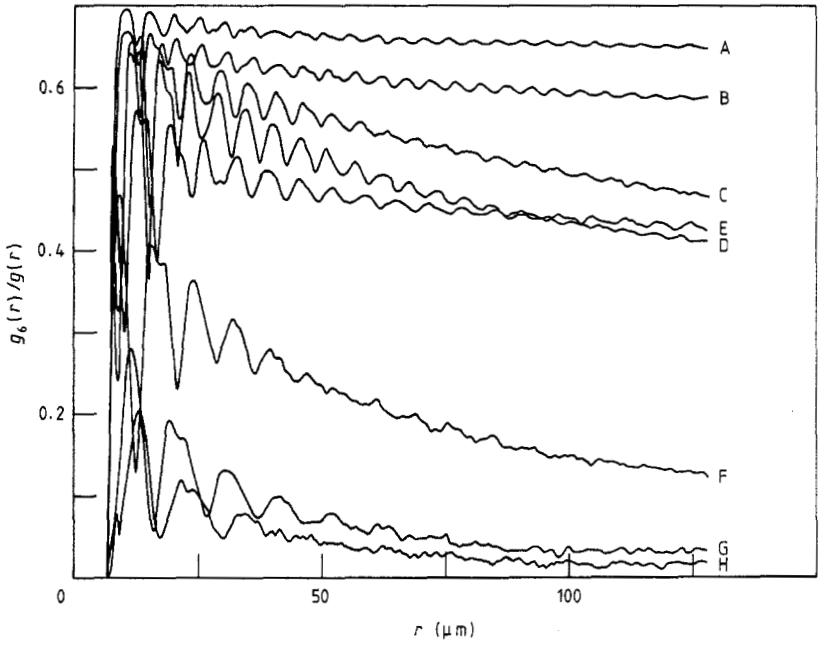

Figure 8. Samples of the average orientational correlation functions $(g_6(r)/g(r))$ from the 2.88 μm sample. The particle numbers for the curves are: A, $N = 867$; B, $N = 829$; C, $N = 650$; $N = 629$; E, $N = 514$; F, $N = 332$; G, $N = 197$; and H, $N = 147$. Curves A through F show power-law decay to zero while G and H display exponential decay. Notice that there is considerable variation in the curves at intermediate densities, as indicated by the crossing of D and E.

where $g(r)$ is the translational correlation function and Ψ_6 is defined by

$$\Psi_6(\boldsymbol{r}) = \frac{1}{N}\sum_{i=1}^{N} \delta(\boldsymbol{r} - \boldsymbol{r}_i)\frac{1}{6}\sum_{j=1}^{6} \exp(\mathrm{i}\delta\theta_{ij}) \tag{9}$$

with θ_{ij} defined as the angle between the ith and the jth particle and some chosen axis.

At very low densities both correlation functions decay rapidly to zero and show increasing order, characterised by slower decay, as the density increases. The correlation lengths for $g(r)$ are determined by fitting the curves with a series of zero-order Bessel functions having exponentially decaying coefficients [22]

$$g(r) = 1 + A_1 \exp(-r/\xi_1)J_0(G_1 r) + A_2 \exp(-r/\xi_2)J_0(G_2 r) + \ldots. \tag{10}$$

Here the A_i are constants, the G_i are proportional to the inverse of the distance to the shells of neighbours and ξ_i are the decay constants. For low densities the correlation functions are fitted well with only one term, and the correlation length is taken as ξ_1. These series expansions duplicate the experimental curves remarkably well, including some of the observed fine structure.

The correlation length or the power-law exponent for the decay of the orientational correlation function is found by fitting the data at large r with decaying exponential or power-law functions. There is some ambiguity in the fit of these data, since often the same data can be fitted with either a power-law or an exponential function. For

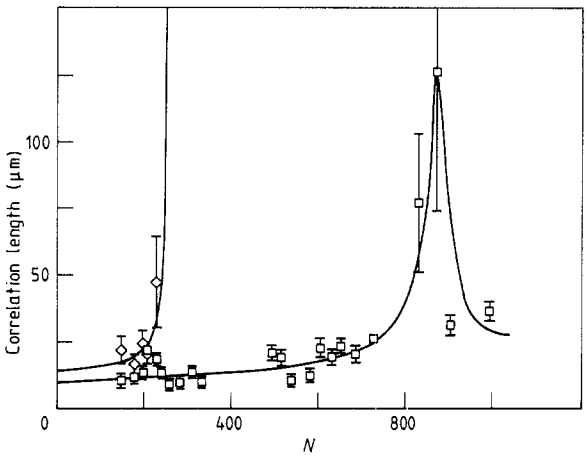

Figure 9. Translational (squares) and orientational correlation (diamonds) lengths for the 2.88 μm sample. Each point is an average over 5 to 20 frames; the error bars are the uncertainty of the fit to these average functions. The orientational correlation functions show power-law decay between the rise in orientational correlation length, $N \simeq 200$, and the rise in translational correlation, $N \simeq 900$. The full curves are guides to the eye.

this reason the behaviour of the orientational correlation function is examined from the low-density side of the transition where the decay is expected to be exponential. A rapid rise or divergence in the correlation length is looked for, and the densities above this apparent divergence are examined with power-law decay fits.

The behaviour of both the translational and orientational correlation lengths as a function of particle number for the 2.88 μm system is shown in figure 9. Each point represents a correlation length obtained from an average of 5 to 20 correlation functions from different regions of the sample. The orientational correlation functions show clear exponential behaviour at very low densities with the correlation length rising abruptly at around $N \simeq 200$ particles. From $N \simeq 400$ to $N \simeq 900$ particles $g_6(r)$ shows power-law behaviour with decay to zero. In this density range the values of the power-law exponents vary substantially from region to region. Notice the crossing of curves D and E in figure 8. We attribute this anomaly to a non-homogeneous distribution of dislocations in the system at the length scale that is sampled.

The corresponding translational correlation length (squares in figure 9) increases slowly with density until $N \simeq 900$ particles at which point it rises abruptly. Above $N \simeq 900$ the correlation length again falls off, showing relatively short-range order. We interpret the rapid rise near $N \simeq 900$ particles as the transition to a solid, and suggest that the fall-off in correlation lengths above this number is the result of compressing the 2D solid which produces internal strain and plastic distortion. The existence of a region of short-range translational correlation and QLR orientational order (appearing in the range $300 < N < 900$, figure 9) is a necessary signature of the hexatic phase.

Samples of average translational and orientational correlation functions from the meniscus data of sample 101B are shown in figures 10 and 11. The translational correlation functions are similar to those of the 2.88 μm system over the entire density range. The orientational correlation functions however, show a distinct difference from those of the 2.88 μm system. For the latter the orientational correlation functions at intermediate densities show a gentle downward slope to zero–power-law decay. In the former (both 101A and 101B), the low-density regions show definite exponential decay to zero while at higher densities the functions change character and show exponential decay to a constant. This change in character occurs in a very narrow region near $N \simeq 900$ particles.

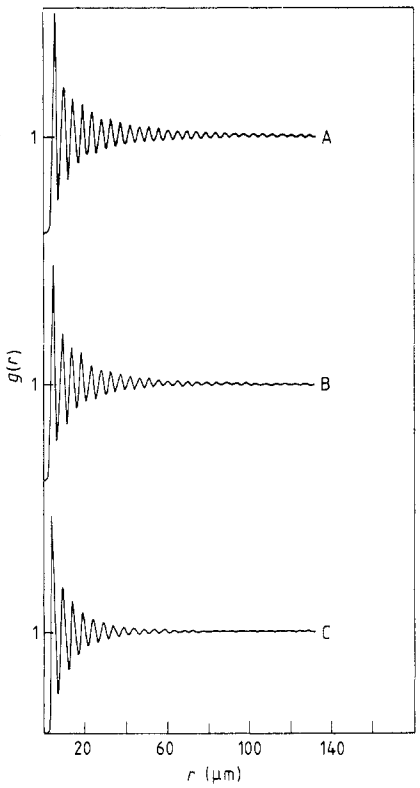

Figure 10. Samples of the average translational correlation functions from the meniscus data of sample 101B. Each curve is the average of five correlation functions. The corresponding particle numbers are: A, $N = 1048$; B, $N = 1002$; and C, $N = 934$.

The correlation lengths of the translational and orientational correlation functions for sample 101B, including both the scan of the density gradient down the meniscus and the barrier compression data, are shown in figure (12) and (13) respectively. Each point represents the average of five individual frames. Both the orientational and translational correlation lengths are approximately equal at low densities and show a slow increase until $N \simeq 900$ particles, at which point they both start to rise rapidly. The meniscus data (squares in figure 12) show a steady increase in correlation length leading to the rapid rise and a peak at $N \simeq 1000$ particles. The translational correlation lengths of the barrier compression data (diamonds in figure 12) parallel the meniscus data at low density, but fail to rise at higher N values. The translational correlation lengths of sample 101A (not shown) also fail to show a substantial increase near the suspected transition.

The orientational correlation lengths for the barrier compression and meniscus data show more agreement (figure 13), with both starting to rise abruptly at $N \simeq 900$ particles. Beyond $N \simeq 940$ particles the orientational correlation functions from the meniscus data can no longer be fitted with exponentials decaying to zero but require exponentials decaying to finite constants: this is an indication of long-range orientational order. In this same region the orientational correlation lengths given by the barrier compression data rise abruptly as well, but are still derived from fits to an exponential function that decays to zero. The orientational correlation lengths of samples 101A and 101B are combined in figure 14. The results appear to be internally consistent.

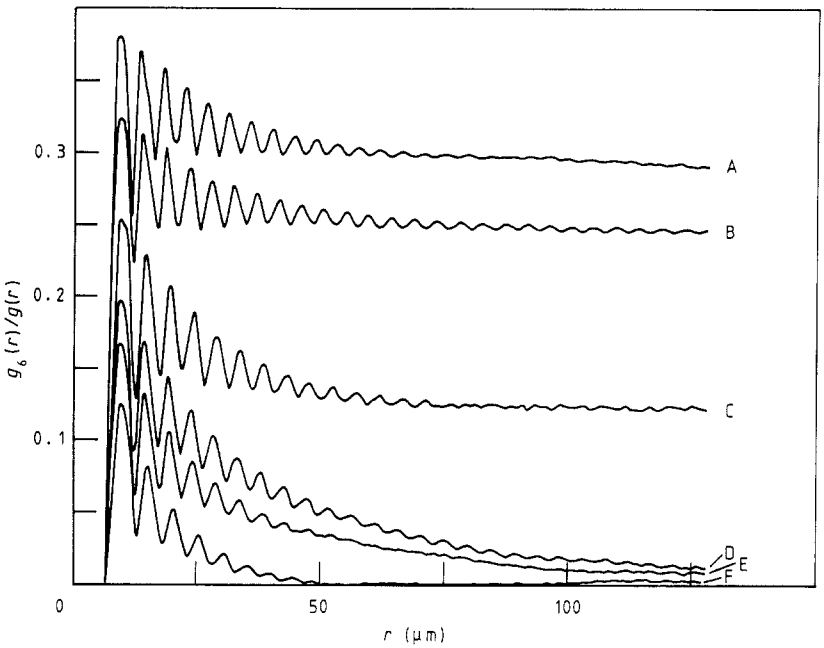

Figure 11. Examples of the average orientational correlation functions from sample 101B. The particle numbers for the curves are: A, $N = 1077$; B, $N = 1002$; C, $N = 934$; D, $N = 965$; E, $N = 932$; and F, $N = 864$. Curves A, B and C are from the meniscus data and decay exponentially to non-zero constants; while D, E and F are curves from the compression data and decay exponentially to zero. Note the difference in behaviour between the two curves with the same approximate particle number.

The failure of the translational correlation length of the 1.01 μm barrier compression data to rise near the suspected transition implies that we may be quenching the system at the transition. We are confident that the meniscus data from the 1.01 μm system is in equilibrium. The simultaneous rise in the orientational correlation lengths of both the barrier compression and meniscus scan data suggests that these systems are not far from equilibrium even very near the transition. Away from the suspected

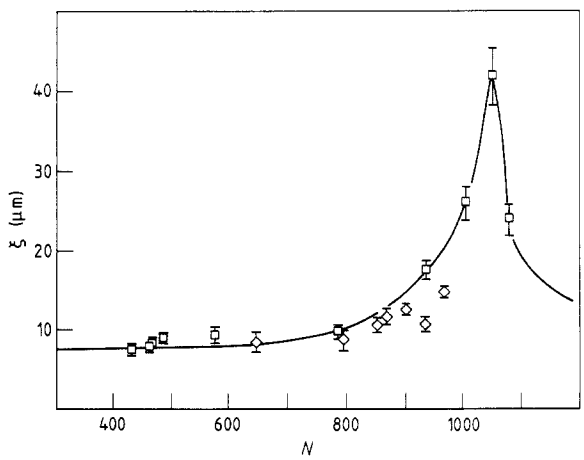

Figure 12. The translational correlation length against the number of particles for sample 101B; each point is the average over five frames. The indicated error is the uncertainty of the fit of these functions. Included are both the meniscus-scan (squares) and the barrier-compression (diamonds) data. The full curve is a guide to the eye.

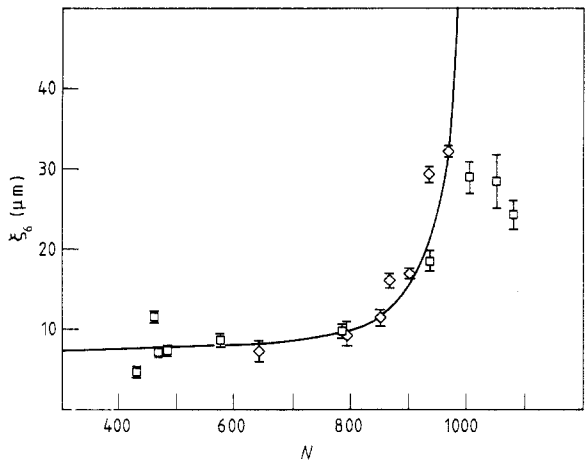

Figure 13. The orientational correlation length ξ_6 against the number of particles for the meniscus-scan (squares) and barrier compression (diamonds) data of sample 101B. Each point is an average of five individual correlation functions; the quoted error is from the uncertainty of the fits. The full curve is a guide to the eye.

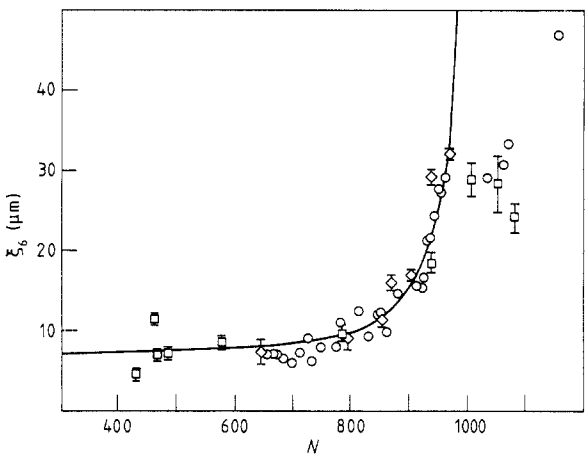

Figure 14. The orientational correlation length ξ_6 against the number of particles for both samples 101A and 101B. The meniscus-scan (squares) and barrier-compression (diamonds) data of sample 101B are averages of five correlation functions; the quoted error is the uncertainty of the fit of these averages. The data from sample 101A (circles) are instantaneous configurations of the system and not averages. The full curve is a guide to the eye.

transition we failed to observe any density gradient, but noted localised short-range density fluctuations with a timescale short compared to that imposed by the moving barriers. This suggests that away from the transition the system was near equilibrium. For the 2.88 μm particles there were no observable density gradients and we were unable to detect any differences between compressions and expansions of the system. This combined with the relatively long times given for the system to relax between compression (expansion) steps, suggest that near-equilibrium was maintained.

4. Discussion

The nature of the defect structure, and the clear presence of QLR orientational order in company with short-range translational order, suggests that the 2.88 μm system melts in a manner consistent with the KTHNY mechanism. This is in contrast to the 1.01 μm systems which show:

(i) a near simultaneous abrupt rise in the orientational and translational correlation lengths at $N \simeq 900$ (5.66×10^6 particles cm^{-2});

(ii) a change in the orientational correlation function from exponential decay to zero, to decay to a constant with no evidence of a power law region;

(iii) a distinctly different nature in the defect structure and its evolution.

This behaviour suggests a change of phase that is consistent with a first order transition. In addition, by viewing the video images of the 1.01 μm sample, one sees a rapid change in behaviour as the system is compressed through those densities where the correlation lengths rise and the slope in the equation of state seems to change. The Brownian motion of the 1.01 μm systems shows an abrupt reduction in amplitude as the density is increased through a narrow density range near $N \simeq 900$. There are also fluctuating disordered areas of lower density surrounded by more ordered regions of higher density, suggesting a narrow range of two-phase coexistence. In contrast, the Brownian amplitude in the 2.88 μm system decreases gradually as the density is increased through the rather broad hexatic phase to the solid phase.

There are interesting groupings of defects in the 2.88 μm sample. In addition to considering pairs of dislocations, interactions among dislocation triplets must also be considered in order to complete the Halperin–Nelson renormalisation procedure. These triplets consist of three bound dislocations whose total Burgers vector is zero. Their formation may be thought of as occurring when one dislocation of a pair, with a Burgers vector along one of the local axes, separates into two distinct dislocations whose Burgers vectors lie along the other two axes. The sum of the two new Burgers vectors equals the Burgers vector of the original dislocation. These dislocations then interact with the remaining original dislocation. A somewhat more complex structure than a triplet is shown in the upper-left-hand corner of figure 6(*c*). Here the interaction is among a quartet of dislocations. Two of these dislocations are isolated and the other two are in contact. The Burgers vectors of the two isolated dislocations are at 60 degrees to each other, and the sum of the Burgers vectors of the dislocations in contact is at 60 degrees to each of those for the isolated defects. Considering the dislocations in contact as a single dislocation, the structure forms a triplet: the total Burgers vector is zero and a Burgers circuit around the structure closes. Evidence of two dislocations combining to form a single dislocation is shown in figure 15. Here two dislocations in the 2.88 μm sample with different Burgers vectors approach and annihilate, leaving a single dislocation. When the two dislocations annihilate, the two Burgers vectors add, leaving a single resultant dislocation. The total Burgers vector is conserved, but the number of dislocations is not. The dissociation of dislocations and the formation of loops of three or more dislocations with a total Burgers vector of zero occurs commonly in the 2.88 μm sample. While the KTHNY theory only includes interactions among dislocation triplets, higher order interactions could be included, and we feel that the above observations are further evidence of KTHNY behaviour.

The major difference in the melting of the 2.88 μm system from the KTHNY theory occurs in the hexatic-to-fluid transition. In the KTHNY theory the hexatic-to-fluid transition should occur with the unbinding of bound disclination pairs (dislocations) to free disclinations via a screening mechanism analogous to that of dislocation unbinding. We clearly do not see a recognisable disclination unbinding in the defect structure. The hexatic-to-fluid transition appears to occur as the result of dislocations interacting to form clusters of defects and grain boundaries. Since a disclination can be composed of a string of dislocations of equal Burgers vectors [25], loss of orientational correlation can occur from the growth of dislocation combinations and clusters. For example, in figure 6(*c*) in the upper-right quadrant there is a small string of four

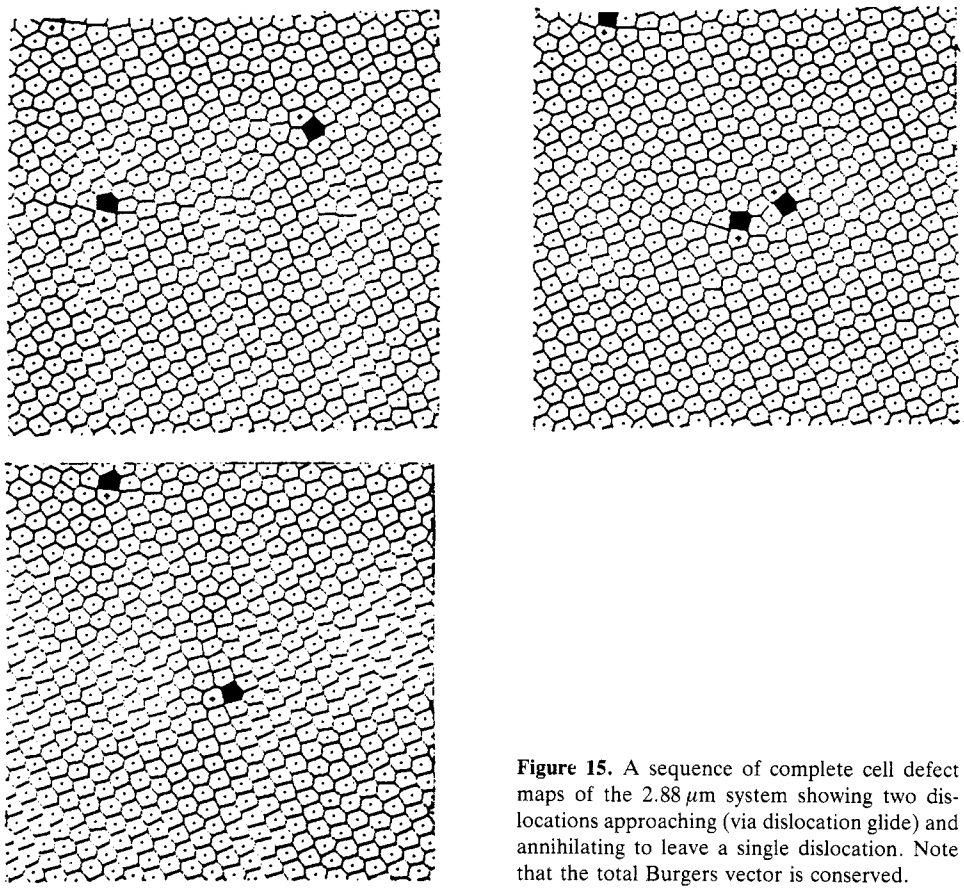

Figure 15. A sequence of complete cell defect maps of the 2.88 μm system showing two dislocations approaching (via dislocation glide) and annihilating to leave a single dislocation. Note that the total Burgers vector is conserved.

dislocations forming a linear chain. The lowermost polygon in the chain is five sided and the uppermost seven sided. If we consider these two polygons as two disclinations unbinding, then the chain of dislocations would represent two disclinations separated by approximately six lattice constants. As other dislocations with the proper Burgers vectors join the chain, they would increase the separation distance between the two opposite disclinations terminating the chain. Such a scenario may have the same effect on the local structure as would the decomposition of individual dislocations to their constituent disclinations in the KTHNY manner.

Finally, the fraction of six-coordinated particles F_6, defined earlier, is displayed in figures 16 and 17. F_6 for the 2.88 μm system (figure 16) climbs very abruptly to around 90% at a very low number density, and then increases gradually as the sample solidifies. In contrast, F_6 climbs much more slowly in the 1.01 μm sample (figure 17) and remains comparatively small, even at high number densities. Consequently, the solid phase of the 2.88 μm sphere system is relatively defect-sparse in comparison to that formed from the smaller spheres. Assuming that the dislocation creation probability obeys a Boltzmann distribution, this suggests that defect-core energies in the two samples may be significantly different, with the 2.88 μm system having a much larger core creation energy than the 1.01 μm system.

If the 1.01μm and 2.88 μm systems do indeed melt via transitions of differing order,

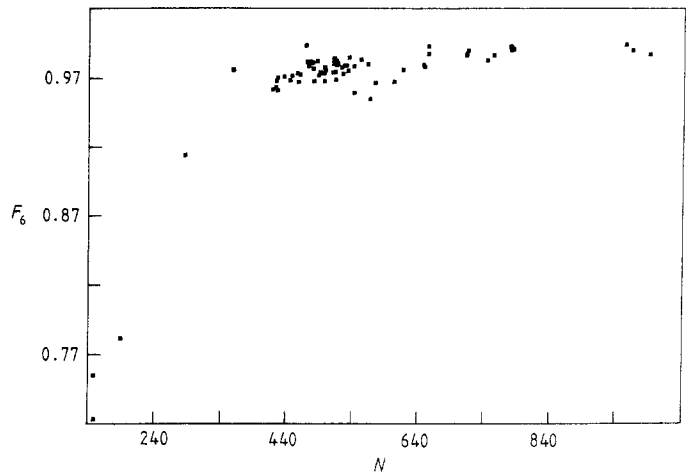

Figure 16. The fraction of six-coordinated particles F_6 against the number of particles for a sequence of individual frames of the 2.88 μm system.

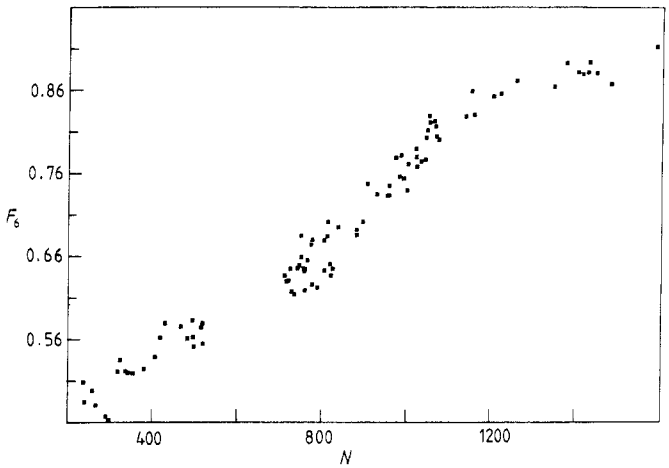

Figure 17. The fraction of six-coordinated particles F_6 against the number of particles for a sequence of individual frames of the 1.01 μm system.

then the above observation may provide the basis for an explanation. If the core energy for the creation of a bound pair in the 1.01 μm sample is small, then the number of dislocation pairs should proliferate as the melting transition is approached. With a large dislocation density the KTHNY renormalisation method loses validity. In this case, one might expect that a model based on Saito's observations [23] could be more appropriate for describing melting in the 1.01 μm sample. On the other hand, if the 2.88 μm system has a high core creation energy as indicated by figure 16, then one expects few dislocations and the system should behave in accord with KTHNY theory.

In conclusion, we have carried out a study of expansion (compression) melting (freezing) in 2D interfacial colloids. We find that the 2.88 μm system displays behaviour consistent with the existence of a hexatic phase and that the 1.01 μm systems appear to melt via a first-order transition. There is circumstantial evidence of a qualitative difference in melting behaviour arising from sphere-size-related differences in the energy required to create bound dislocation pairs. The significance of this evidence is mitigated somewhat by the presence of numerous multiparticle defects in the samples

formed with 1.01 μm diameter microspheres. Such impurities may lower the core creation energy and enhance the production of defects.

Acknowledgments

We thank Matt Glaser, Rainer Malzbender and Yeke Tang for helpful discussions and comments. This work was supported by the US Department of Energy Grant No DE-FG02-86ER45236.

References

[1] Kosterlitz J M and Thouless D J 1973 *J. Phys. C: Solid State Phys.* **6** 1181
[2] Kosterlitz J M 1974 *J. Phys. C: Solid State Phys.* **7** 1046
[3] Halperin B I and Nelson D R 1978 *Phys. Rev. Lett.* **41** 121
[4] Nelson D R and Halperin B I 1979 *Phys. Rev.* B **19** 2457
[5] Young A P 1979 *Phys. Rev.* B **19** 1855
[6] Mermin N D 1968 *Phys. Rev.* **176** 250
[7] Ramakrishnan T V and Yussouff M 1979 *Phys. Rev.* B **19** 2775
Ramakrishnan T V 1982 *Phys. Rev. Lett.* **48** 514
[8] Chui S T 1983 *Phys. Rev.* B **28** 178
[9] Venkataramen G and Sahoo D 1985 *Pramana* **24** 317
Strandburg K J 1988 *Rev. Mod. Phys.* **60** 161
[10] Broughton J Q, Gilmer G H and Weeks J D 1982 *Phys. Rev.* B **25** 4651
[11] Bakker A F, Bruin C and Hilhorst H J 1984 *Phys. Rev. Lett.* **52** 449
Bakker A F, Bruin C, van Dieren F and Hillhorst H J 1982 *Phys. Lett.* **93A** 67
[12] Toxvaerd S 1981 *Phys. Rev.* A **24** 2735
[13] DeVille G, Valdes A, Andrei E Y and Williams F I B 1984 *Phys. Rev. Lett.* **53** 588
[14] Rosenbaum T F, Nagler S E, Horn P M and Clarke R 1982 *Phys. Rev. Lett.* **50** 1791
[15] Heiney P A, Birgeneau R J, Brown G S, Horn P M, Moncton D E and Stephens P W 1982 *Phys. Rev. Lett.* **48** 104
[16] Nagler S E, Horn P M, Rosenbaum T F, Birgeneau R J, Sutton M, Mochrie S G J, Moncton D E and Clarke R 1985 *Phys. Rev.* B **32** 7373
[17] Kjaer K, Als-Nielsen J, Laxhuber C A and Möhwald H 1987 *Phys. Rev. Lett.* **58** 2224
[18] Dutta P, Peng J B, Lin B, Ketterson J B, Prakash M, Georgopoulos P and Ehrlich S *Phys. Rev. Lett.* **58** 2228
[19] Pindac R, Moncton D E, Davey S C and Goodby J W 1981 *Phys. Rev. Lett.* **46** 1134
[20] Moncton D E, Pindac R, Davey S C and Brown G S 1982 *Phys. Rev. Lett.* **49** 1863
[21] Murray C A and Van Winkle D H 1987 *Phys. Rev. Lett.* **58** 1200
[22] Tang Y, Armstrong A J, Mockler R C and O'Sullivan W J *Phys. Rev. Lett.* submitted
[23] Saito Y 1982 *Phys. Rev. Lett.* **48** 1114
Saito Y 1982 *Phys. Rev.* B **26** 6239
[24] Kleinert H 1982 *Phys. Lett.* **89A** 294
[25] Kleinert H 1983 *Phys. Lett.* **95A** 381
[26] Pieranski P 1983 *Contemp. Phys.* **24** 25
[27] Chan D Y C, Henry J D and White L R 1981 *J. Colloid Interface Sci.* **79** 410
[28] Earnshaw J C 1986 *J. Phys. D: Appl. Phys.* **19** 1863
[29] Dyrdal I 1986 *J. Appl. Phys.* **60** 1913
[30] Pieranski P 1980 *Phys. Rev. Lett.* **45** 569
[31] Hurd A J 1985 *J. Phys. A: Math. Gen.* **18** L1055
[32] Stillinger F H Jr 1961 *J. Chem. Phys.* **35** 1584
[33] van Swol F and Woodcock L V 1980 *J. Chem. Phys.* **73** 913
[34] Kalia R K and Vashishta P 1981 *J. Phys. C: Solid State Phys.* **14** L643
[35] McTague J P, Frenkel D and Allen M P 1980 *Ordering in Two Dimensions* ed. S K Sinha (Amsterdam: North-Holland) p 147
[36] Rubinstein M and Nelson D R 1982 *Phys. Rev.* B **26** 6254